Available online at www.sciencedirect.com
ScienceDirect
Journal of Computational Physics 220 (2006) 355–382
JOURNAL OF COMPUTATIONAL PHYSICS
www.elsevier.com/locate/jcp

On the use of a high order overlapping grid method for coupling in CFD/CAA

G. Desquesnes [a,*], M. Terracol [a], E. Manoha [a], P. Sagaut [b]

[a] Office National d'Etudes et de Recherches Aérospatiale, DSNA, BP 72, 29 av Division Leclerc, 92322 Châtillon, France
[b] Université Paris VI, LMM – UPMC/CNRS, Boite 162, 4 place Jussieu, 75252 Paris cedex 05, France

Received 3 June 2005; received in revised form 17 February 2006; accepted 15 May 2006
Available online 7 July 2006

Abstract

This paper presents a theoretical analysis and two applications of a high-order overlapping grid method for coupling Cartesian and curvilinear grids, developed in order to simulate aerodynamic noise. First, the overlapping grid method based on Lagrange interpolating polynomials is described and a theoretical analysis of the interpolation operator is then carried out. It shows that the interpolation generates spurious modes that depend on the wavenumbers of the signal. Besides it also gives the optimal conditions in which interpolation can be applied. Then an application to the simulation of the aeroacoustic noise generated by the vortex shedding behind a cylinder is presented. During this simulation, it appears that interpolation can create some spurious acoustic modes in regions where hydrodynamic fluctuations are significant, as predicted by the theoretical analysis. It is shown that these spurious modes disappear when a refined Cartesian grid is used (26 points per wavelength of the vortex shedding were found to be adequate in this study). At last, the simulation of the aerodynamic noise of a three element high-lift wing profile has then been carried out. For this application, the main acoustic source at the slat trailing edge is represented analytically. The propagation of the generated acoustic wave is simulated with a mean flow at rest and with a steady turbulent mean flow computed by RANS. The first application allows us to assess the method by comparing the results to a reference solution. The second one shows that the influence of a non-uniform mean flow on the directivity of an acoustic source can be observed in complex geometries. This application therefore shows that the proposed coupling method is well adapted to complex geometries that are usually met in industrial applications.

AMS: 65C20; 76Q05

Keywords: Aeroacoustics; Propagation; High order schemes; Overlapping grid method; CFD/CAA coupling

* Corresponding author. Tel.: +33 1 46 734246; fax: +33 1 46 734166.
E-mail address: guillaume.desquesnes@onera.fr (G. Desquesnes).

0021-9991/$ - see front matter © 2006 Elsevier Inc. All rights reserved.
doi:10.1016/j.jcp.2006.05.019

1. Introduction

Computational AeroAcoustics (CAA) is a science in rapid development these last years following the demand of aeronautic industries. One of the main purposes is to be able to simulate the generation and propagation of aerodynamic noise.

Our purpose is to predict with accuracy the flow around a body and to compute the farfield noise generated by this flow. The difficulty comes from the disparity of scales to simulate, the hydrodynamic and acoustic scales being very different. To achieve this purpose, Manoha et al. [1] have proposed a hybrid method in three steps. The first one consists in simulating the flow near the body with an unsteady simulation (DNS/LES) to describe accurately the aerodynamic noise sources. Then, on a second domain, Euler equations written in perturbation form are used to simulate the propagation of sound waves in a midfield domain where the turbulence rate is low but mean flow gradient are still significant. It has to be noted that for this second step, some high-order numerical schemes have to be introduced to allow a correct propagation of the acoustic waves. More particularly, the scheme has to minimize the dissipative and dispersive numerical errors. In the last step, when the mean flow is nearly uniform, an integral method is utilized to compute the acoustic radiation in the farfield.

An accurate simulation of the flow around the body requires a fine body-fitted grid. On the second domain, a good propagation of the acoustic waves requires an homogenous and isotropic grid, together with the use of some high-order numerical schemes. In this aim, a first approach has been to develop a grid refinement method to adapt the body-fitted grid to acoustic wave propagation as we further off the body. Guénanff et al. [2–4], developed such an approach, which has been assessed on several configurations. But these applications have also shown the limits of such an approach. Indeed, the extension from 2D to 3D is not straightforward and it is difficult to use it on geometrically complex configurations since curvilinear grids are required. In the same time, new methods based on another strategy have been proposed in recent works by Defls [5], Sherer and Scott [6], Lee and Baeder [7]: Chimera type methods well suited for CAA. They are based on previously developed Chimera methods for CFD [8–10], but higher order interpolations have to be used to match the accuracy requirement of CAA. The difference between all these recent overset or overlapped grid techniques relies on the numerical schemes that are used (spatial derivation, filtering, temporal integration, interpolation), while the way to proceed remains the same for all of them. It consists in defining a mesh coupling method for curvilinear and Cartesian grids. Such an approach has two main interests. The first one is to benefit of the numerical properties of Cartesian grid for propagation and those of body-fitted mesh for geometrically complex boundary conditions as clearly stated by Delfs [11]. The second one is its flexibility since it renders the use of structured grids for complex geometry much easier [10,9,5]. Previous results were mostly dealing with simple test cases and the definition of a method well suited for complex flow is still an open issue. In most cases, the mean flow of the simulations is at rest, and the nature of the studied phenomenons is purely acoustic. Yin and Delfs presented a simulation where the mean flow was not uniform but was analytically defined [12]. Therefore, the present work investigates the use of overlapping grid method of Chimera type on some more complicated configurations. In these cases, the increased complexity has two possible origins: the disparity between acoustic and hydrodynamic scale, the geometry of the configuration. Two particular cases, involving such difficulties, will be considered in this paper: the simulation of the noise created by the flow around a cylinder and the simulation of the radiation of an aeroacoustic source of a high lift wing profile in landing configuration. The first application will show that interpolation can create spurious acoustic modes. In order to understand this phenomenon, a theoretical analysis of Lagrange polynomials (used in the coupling method) has been carried out. It is different from one proposed by Tam and Kurbatskii [13] and then used by Sherer and Scott [14]. This study allows us to understand the origin of the spurious modes created by the interpolant and what is the influence of the order of interpolation on the magnitude of these modes. Besides, this analysis gives us the condition in which the spurious modes can be filtered. The paper is organized as follows: In Section 2, the equations for CAA, the numerical methods for spatial derivation, filtering and temporal integration are presented. Then, the overlapping grid method is defined. In Section 3, a theoretical analysis of the interpolation based on Lagrange polynomials is performed within the framework of signal theory. Section 4 shows an application of the coupling method to the simulation of the aerodynamic noise generated by the vortex shedding behind a cylinder. For this application, it is observed that the interpolation procedure is respon-

sible for spurious acoustics sources, and thanks to analysis previously done, an explanation of this phenomenon is proposed. At last in Section 5, the overlapping grid method will be applied to an industrial case: the propagation of an acoustic wave around a high lift wing profile in landing configuration. A first simulation is done with a mean flow at rest to assess the method by comparing the results to those obtained with a simulation based on BEM (Boundary Element Method). Then, a steady mean flow computed by RANS is used as a mean flow, therefore making it possible to investigate the effects of the flow on the acoustic propagation.

2. Equations and numerical method

2.1. Basic equations

We consider the compressible Navier–Stokes equations under the following compact form:

$$\frac{\partial U}{\partial t} + \mathscr{C}(U) = \mathscr{V}(U) \tag{1}$$

where $U = (\rho, \rho\boldsymbol{u}^{\mathrm{T}}, \rho E)^{\mathrm{T}}$ is the conservative variable vector, with $\boldsymbol{u} = (u, v, w)^{\mathrm{T}}$ the velocity vector. The convection term is expressed as:

$$\mathscr{C}(U) = \begin{pmatrix} \nabla \cdot (\rho \boldsymbol{u}) \\ \nabla \cdot (\rho \boldsymbol{u} \otimes \boldsymbol{u}) + \nabla p \\ \nabla \cdot ((\rho E + p)\boldsymbol{u}) \end{pmatrix} \tag{2}$$

where p is the pressure, ρ the density, $\boldsymbol{u}$ the velocity vector and ρE the total energy.

The viscous terms are:

$$\mathscr{V}(U) = \begin{pmatrix} 0 \\ \nabla \cdot \sigma \\ \nabla \cdot (\sigma : \boldsymbol{u}) - \nabla \cdot Q \end{pmatrix} \tag{3}$$

Some classical expressions are retained for the viscous stress tensor σ and viscous heat flux vector Q, *i.e.*:

$$\sigma = 2\mu S^d \tag{4}$$

$$Q = \kappa \nabla T \tag{5}$$

where the exponent d denotes the deviatoric part of a tensor, T is temperature, and S is the rate-of-strain tensor:

$$S = \frac{1}{2}(\nabla \boldsymbol{u} + (\nabla \boldsymbol{u})^{\mathrm{T}}) \tag{6}$$

The temperature is linked to the pressure by the perfect gas state-law, and Sutherland's law is used to compute the viscosity μ as a non-linear function of T. Finally, the thermal conductibility coefficient κ is linked to viscosity through the use of a Prandtl number assumption ($Pr = 0.7$ in this study) as: $\kappa = C_p\mu/Pr$, where C_p is the iso-pressure heat coefficient.

Obviously, the set of the Euler equations correspond to the case in which the viscous term $\mathscr{V}(U)$ is neglected.

2.2. Navier–Stokes perturbation equations (NSPE)

As it is usually the case in aeroacoustics, the basic equations describing the flow dynamics will be solved in a perturbation form. The principle of this method is to decompose the global field U as a mean part U_0 – that is considered as an input of the problem – and a fluctuating one U':

$$U = U_0 + U' \tag{7}$$

The evolution equations for the mean field are:

$$\frac{\partial U_0}{\partial t} + \mathscr{C}(U_0) = \mathscr{V}(U_0) + S_0 \tag{8}$$

where S_0 is an additive source term in the equations which accounts for the fact that the mean field U_0 is not necessary an exact solution of the original Navier–Stokes equations. For instance, this term can be related to the modelling terms arising from the use of a turbulence model (RANS, LES). One can remark here that the particular case of a steady mean flow corresponds to $S_0 = \mathscr{C}(U_0) - \mathscr{V}(U_0)$.

The evolution equations for the perturbation field U' that will be considered in the following are then simply obtained by subtracting these last equations from the full Navier–Stokes equations (Eq. (1)):

$$\frac{\partial U'}{\partial t} + \mathscr{C}(U' + U_0) - \mathscr{V}(U' + U_0) = \mathscr{C}(U_0) - \mathscr{V}(U_0) - S_0 \tag{9}$$

where the r.h.s. theoretically vanishes in the case of a steady mean flow U_0. It is however recommended to compute explicitly this term in the formulation, in order to account for some possible convergence and/or discretization errors. Solving the set of equations (9) instead of the full Eq. (1) has the double advantage that it minimizes the sensitivity of low-amplitudes perturbations to numerical errors, and that an arbitrary mean field can be imposed. In the following, this set of equations will be referred to as the Navier–Stokes perturbation equations (NSPE).

It is to be noted that this method, originally proposed by Morris [15] and referred to as the non-linear disturbance equations (NLDE) approach, was also extended to the case of the filtered Navier–Stokes equations solved in large-eddy simulation (LES) by Labourasse and Sagaut [16]. In this last case, the field was then decomposed as a mean field U_0 computed by RANS, and a fluctuating part U' computed by LES.

2.3. Numerical method

In this study, since the objective is to simulate noise propagation, some high-order numerical schemes have been retained to discretize the NSPE (9).

The spatial scheme used in this study relies on a classical sixth-order accurate finite-difference centered discretization. The spatial derivatives of any quantity f are then computed as (in one dimension):

$$\frac{\partial f}{\partial x}(x) = \frac{1}{\Delta x}\sum_{k=-3}^{3} a_k f(x + k\Delta x) \tag{10}$$

where Δx is the space step in the x-direction. The coefficients values are, respectively, $a_0 = 0$, $a_1 = -a_{-1} = 45/60$, $a_2 = -a_{-2} = -9/60$, $a_3 = -a_{-3} = 1/60$. A Fourier analysis of this scheme shows that eight points per wavelength are necessary for a satisfactory approximation of the derivative operator [17,18]. For curvilinear grids, the curvilinear extension strategy proposed by Visbal and Gaitonde [19] has been retained.

Since this centered scheme is non-dissipative, it promotes the growth of spurious high-frequency numerical errors. For this reason, a stabilization step is also added in the numerical method, which relies on the application of a 10th-order accurate centered linear filtering operator on the solution at each time step. This filtering operator F is defined as (in one dimension):

$$F(f)(x) = \sum_{k=-5}^{5} b_k f(x + k\Delta x) \tag{11}$$

To compute the filter coefficient values, the first condition imposed to the coefficients is that the filter suppresses the odd–even mode. This constraint leads to the following expression:

$$\sum_{k=-5}^{5} b_k (-1)^k = 0$$

This equation has 5 degrees of freedom which are then used to maximize the order of the filtering operator. To do so, the Taylor series expansion of $f(x + k\Delta x)$ is written for $k = -5, \ldots, 5$, and the filter coefficients are then computed so that:

$$F(f)(x) = f(x) + \mathcal{O}(\Delta x^{10})$$

The filter coefficient values are determinated by inversing a system of six equations and are, respectively:

$$b_0 = 772/1024, \quad b_1 = b_{-1} = 210/1024, \quad b_2 = b_{-2} = -120/1024, \quad b_3 = b_{-3} = 45/1024,$$
$$b_4 = b_{-4} = -10/1024, \quad b_5 = b_{-5} = 1/1024$$

It is to be noticed that the degrees of freedom could be used in another purpose as Bogey and Bailly [20] have proposed it.

On uniform Cartesian grids, the filtering operator in two or three dimensions is simply obtained by recursive application of the filter in each direction. For instance in two dimensions, the filtering operator is defined as:

$$F(f)(x,y) = \sum_{k=-5,5} \sum_{l=-5,5} b_k b_l f(x + k\Delta x, y + l\Delta y) \tag{12}$$

For curvilinear grids, the way to proceed is the following. The two-dimensional case is considered here for the sake of simplicity without restriction on the generality of the method. Let g be a function to be filtered at the points $(x_{i,j}, y_{i,j})$ of a mesh. The filtering operator G is defined as follows:

$$G(g)(x_i, y_j) = \sum_{k=-5,5} \sum_{l=-5,5} b_k b_l g(x_{i+k,j+l}, y_{i+k,j+l}) \tag{13}$$

This filter is of the 10th order in the computational domain used to solve the fluid mechanics equations. Indeed let h be the transformation such that:

$$(x_{i,j}, y_{i,j}) = h(i,j)$$

The corresponding computational domain is a Cartesian grid with $\Delta x = 1$ and $\Delta y = 1$. So Eq. (13) is equivalent to:

$$G(g)(x_i, y_j) = \sum_{k=-5,5} \sum_{l=-5,5} b_k b_l g(h(i+k, j+l))$$
$$\Longleftrightarrow$$
$$G(g)(x_i, y_j) = \sum_{k=-5,5} \sum_{l=-5,5} b_k b_l f(i+k, j+l) \tag{14}$$

with

$$f(i,j) = g(h(i,j)) = g(x_{i,j}, y_{i,j})$$

The definition of G can then be extended to every point of the physical domain. Let (x,y) be a point of this domain, there exists (ξ,η) such that:

$$(x,y) = h(\xi,\eta)$$

The filtering operator G applied to g in the (x,y) space can then be written as:

$$G(g)(x,y) = \sum_{k=-5,5} \sum_{l=-5,5} b_k b_l f(\xi + k, \eta + l) \Longleftrightarrow G(g)(x,y) = \sum_{k=-5,5} \sum_{l=-5,5} b_k b_l g(x + \alpha_{x,y,k,l}, y + \beta_{x,y,k,l})$$

with

$$(\alpha_{x,y,k,l}, \beta_{x,y,k,l}) = h(\xi + k, \eta + l) - h(\xi, \eta)$$

It is to be noticed that:

$$G(g)(x,y) = F(f)(\xi,\eta)$$

The filtering process on curvilinear mesh is therefore of the 10th order in the computational domain since it is of the same form as Eq. (12). However, this does not imply that it is of the 10th order in the physical domain. The resulting scheme is quite classical in aeroacoustics, and has been extensively used for both aerodynamic and acoustic computations (see Terracol et al. [21]). However, it is important to notice that: (i) It is a high

accuracy scheme. This involves that the interpolation operator used to perform the CFD/CAA coupling must preserve as much as possible this property; (ii) The stencil of the scheme is quite large since it requires five discretization points on each side of the point to be computed. That means that attention has to be paid to the fact that the overlapping area between the CFD and CAA regions has to be wide enough to allow a proper application of the spatial scheme on both the two domains.

Finally, a compact third-order accurate Runge–Kutta scheme has been used for time advancement.

2.4. Description of the coupling method

The method presented here is a simplified overlapping grid technique. Indeed, for the two following applications, the phenomena of production and diffraction of the acoustic wave will take place in the curvilinear domain only. In this condition, the acoustic information has just to be transmitted in one way, from the curvilinear domain to the Cartesian one. Therefore, only a one-way coupling method based on overlapping grid will be considered here. The configuration is the following: a body fitted grid is used around the solid (cylinder, airfoil, ...) along with a Cartesian overlapping mesh (see Fig. 1). Then a boundary is defined on the curvilinear mesh: what is inside the boundary will be simulated on the body fitted grid, while outside information will be computed on the Cartesian one. In such a configuration, acoustic production and diffraction phenomena only take place in the curvilinear domain and the Cartesian grid computation has just to propagate the acoustic waves. This one-way coupling method by grid overlap can be seen as a particular boundary condition treatment for the Cartesian mesh [22]. Because of possible numerical reflections, the curvilinear mesh cannot end at the coupling boundary. It extends beyond the interface between the two domains and this part constitutes a sponge zone.

Cartesian points in an inside band of the boundary between the two domains therefore play the role of ghost points used in classical boundary treatment. Before each time step and filtering process, the values at these Cartesian points must be interpolated. The width of the band depends on the order of the schemes that are used. In each direction, the number of points must be at least $\max((n_d - 1)/2, (n_f - 1)/2)$ with n_d the stencil width of the spatial derivative scheme and n_f the stencil of the discrete filter – n_d and n_f being odd numbers. Before defining the interpolation method, one notice that, on the contrary of most overlapped or overset grid methods [11,22], the Cartesian points inside the coupling boundary that do not play the role of ghost points are not discarded here. This step is usually called ''hole cutting process'' and the purpose is to ''remove'' the points where the flow has not physical sense. These points are not identified here for two reasons:

- the flow computed in these points does not have physical sense, but it has no effect on the flow computed on the other Cartesian points;
- the computer used in our study has a vectorized architecture, so removing points of a domain has negative effect on CPU performance.

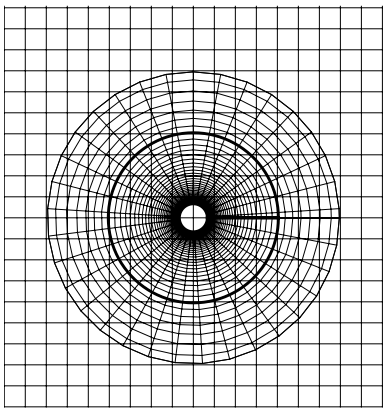

Fig. 1. Cartesian and body-fitted grids, the thick line is the interface.

The issue of choosing an appropriate interpolation operator for aeroacoustics applications has already been investigated in several studies for instance in Delfs [11], Sherer and Scott [14], Guénanff et al. [3], Tam and Kurbatskii [13]. The conclusions of the studies of Sherer and Scott, and Guénanff et al. are the same: explicit Lagrange interpolator has globally given the best results on the test configurations. In his conclusion, Guénanff has precised that the fourth order interpolator was a good compromise between accuracy and computational cost. This operator has thus been retained as a basis for the present approach. The interpolation problem consists in determining the value of a function f at any point M of a geometric space knowing its values only at the points $P_{i,j}$ of a structured mesh. Because we perform interpolation, there exists a quadrangle $(P_{i,j}; P_{i+1,j}; P_{i+1,j+1}; P_{i,j+1})$ to which the point M belongs (see Fig. 2). The value of f at M is evaluated knowing $f_{i+k,j+l}$, $(k,l) \in [-1,2]^2$, the values of f at points $P_{i+k,j+l}$. We cannot use Lagrange polynomials of the 3rd degree on this configuration. Therefore, we consider the geometrical transformation h such that the image of $P_{i+k,j+l}$ by h is (k,l). This new space is usually called the computational domain. The same space is used to solve the equations that are considered on curvilinear meshes. The issue of determining the coordinates (X, Y) of M in this space is a classical problem in Chimera-like methods. The approach used by Sherer and Scott [6] or Delfs [11] is a high-order extension of the method employed by Benek [23]. It consists in using the interpolator to approximate the function h^{-1}. Then an iterative Newton method is used in order to inverse h^{-1} at the point M. The approach proposed by Guénanff et al. and retained here is different. The transformation h is approximated as a polynomial function of the third-order for each coordinate (in two dimensions):

$$h(x,y) = (h_X(x,y), h_Y(x,y))$$

with

$$h_X(x,y) = \sum_{k=0}^{3}\sum_{l=0}^{3} a_{k,l}x^k y^l$$

$$h_Y(x,y) = \sum_{k=0}^{3}\sum_{l=0}^{3} b_{k,l}x^k y^l$$

The coefficients a and b are determinated such that:

$$h(P_{i+k,j+l}) = (k,l) \quad \text{for } (k,l) \in [-1,2]^2$$

This leads to a linear system of equations. The coefficients a and b are determinated by inverting this system. Then the coordinates (X, Y) of the point M can be computed. The interpolation of f at the point M, noted $\mathcal{I}(f)(M)$, is computed as:

$$\mathcal{I}(f)(M) = \sum_{k=-1}^{2}\sum_{l=-1}^{2} f_{i+k,j+l}P_k(X)P_l(Y) \tag{15}$$

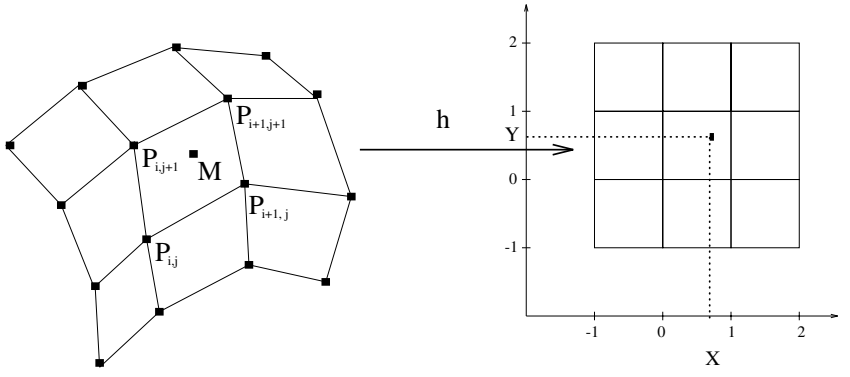

Fig. 2. Interpolation of the point M in the reference grid.

where

$$P_k(x) = \prod_{\substack{p=-1 \\ p\neq k}}^{2} \frac{x-p}{k-p} \tag{16}$$

It is well known that this interpolation of f at the point M is fourth order accurate in the computational domain. This result tells us that the finer is the mesh the better is the interpolation but does not provide give with more information about the interpolation error in function of the wavenumbers of the signal.

3. Theoretical analysis of Lagrange interpolation

The interpolation defined above in the Cartesian reference space in two dimensions comes from the tensorisation of the 1D interpolation scheme. Therefore, the theoretical study is performed in 1D. The results can then be extended in 2D in a straightforward manner. This analysis is different from the one proposed by Tam and Kurbatskii [13] and extended by Sherer and Scott [6] in which they developed optimized interpolation methods. Our theoretical analysis is made within the framework of the signal theory and can be extended to the main interpolation methods.

Interpolation is used to initialize values on a mesh from the data coming from another one. In this process, two stages will be distinguished: first the construction of a continuous signal from the sample signal and, second, the discretization of this continous signal on a new mesh. We will understand then how interpolation can create spurious modes.

3.1. The fundamental result of the signal theory

Let x_n be the points of an infinite mesh, $x_n = n\Delta x$ with n positive or negative integer. Let f be a square integrable function. Its Fourier transform $\hat{f}$ is defined as:

$$\hat{f}(\alpha) = \int_{-\infty}^{\infty} f(x)\mathrm{e}^{-\mathrm{i}\alpha x}\,\mathrm{d}x \tag{17}$$

where α is the wavenumber. Following the signal theory, the function f discretized at the mesh points is written as a sum f_d of Dirac distributions:

$$f_d(x) = \sum_{n=-\infty}^{\infty} f(n\Delta x)\delta(x - n\Delta x) \tag{18}$$

The fundamental result of the signal theory is Shannon [24] and Whitaker's [25] theorem: if the support of $\hat{f}$ is included in $]-\pi/\Delta x, \pi/\Delta x[$ then

$$f(x) = \sum_{n=-\infty}^{\infty} f(n\Delta x)h_{\Delta x}(x - n\Delta x) \tag{19}$$

$$\Longleftrightarrow$$

$$f(x) = f_d \star h_{\Delta x}(x) \tag{20}$$

where

$$h_{\Delta x}(x) = \frac{\sin(\pi x/\Delta x)}{\pi x/\Delta x} \tag{21}$$

This theorem shows that $h_{\Delta x}$ is the ideal interpolation function. In practice, we cannot use it because the exact value of $f(x)$ is defined as an infinite sum.

3.2. Lagrange interpolation and signal theory

We keep the signal theory hypothesis and assume that Shannon and Whitaker's theorem can be applied to f. The interpolation of f at any location of x with 3rd degree Lagrange polynomials can be written:

$$\mathscr{I}(f)(x) = \sum_{n=-\infty}^{\infty} 1_{[0,1[}\left(\frac{x}{\Delta x} - n\right) \sum_{k=-1}^{2} f_{n+k} P_k\left(\frac{x}{\Delta x} - n\right) \tag{22}$$

where

$$1_{[0,1[}(x) = \begin{cases} 1 & \text{if } x \in [0,1[\\ 0 & \text{else} \end{cases} \tag{23}$$

and $P_k(x)$ was defined in Eq. (16). By rewriting Eq. (22), one can prove that it is equivalent to:

$$\mathscr{I}(f)(x) = f_d \star c_{\Delta x}(x) \tag{24}$$

where

$$c_{\Delta x}(x) = \sum_{k=-1}^{2} P_k\left(\frac{x}{\Delta x} + k\right) 1_{[0,1[}\left(\frac{x}{\Delta x} + k\right) \tag{25}$$

Interpolation relying on Lagrange polynomials is therefore equivalent to a convolution. One can notice that Eqs. (20) and (24) are of the same form. In a more general case, the signal theory predicts that every linear and steady operator can be written as a convolution product [26]. Fig. 3 displays $h_{\Delta x}$ and $c_{\Delta x}$ for $\Delta x = 1$, we can notice that $c_{\Delta x}$ is an approximation of $h_{\Delta x}$. Indeed, the higher is the order of the Lagrange polynomials used, the more similar is $h_{\Delta x}$ to $c_{\Delta x}$: pieces of curve appear around the central peak of $h_{\Delta x}$ that come to "stick" to $c_{\Delta x}$. Thanks to Eq. (24), one can derive an explicit relation between $\widehat{\mathscr{I}(f)}$ and $\hat{f}_d$. Indeed, in Fourier space, Eq. (24) is equivalent to:

$$\widehat{\mathscr{I}(f)}(\alpha) = \hat{f}_d(\alpha)\hat{c}_{\Delta x}(\alpha) \tag{26}$$

One can see that all the features of the interpolation depend on $\hat{c}_{\Delta x}$. Fig. 4 displays $\hat{c}_{\Delta x}$ and $\hat{h}_{\Delta x}$. Several remarks can be drawn from this figure. First, both $\hat{h}_{\Delta x}$ and $\hat{c}_{\Delta x}$ are real functions. That means that the interpolation itself does not create dephasing, this property comes from the symmetry of $c_{\Delta x}$. Secondly, $\hat{c}_{\Delta x}(\alpha) \leqslant \Delta x$ for every α ($\Delta x = 1$ in Fig. 4), interpolation based on Lagrange polynomials does not magnify some components of the original spectrum. Third, the magnitude of the high wavenumbers is lowered, $\hat{c}_{\Delta x}(\pi/\Delta x) = \Delta x/2$. At last, the support of $\hat{c}_{\Delta x}$ is not included in $]-\pi/\Delta x, \pi/\Delta x[$ and Poisson's formula [26] shows that:

$$\hat{f}_d(\alpha) = \frac{1}{\Delta x} \sum_{n=-\infty}^{\infty} \hat{f}\left(\alpha - \frac{2\pi n}{\Delta x}\right) \tag{27}$$

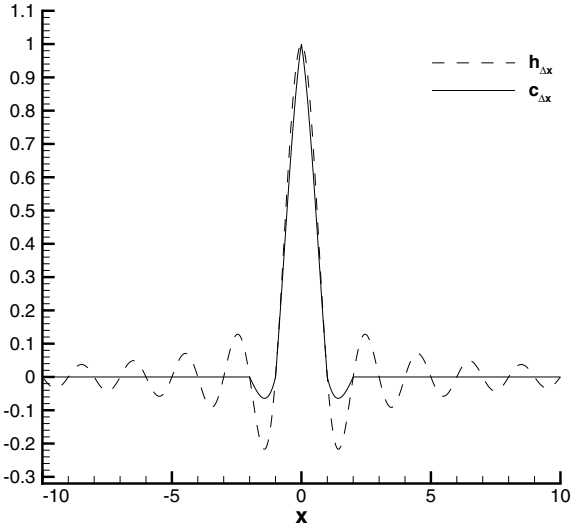

Fig. 3. $c_{\Delta x}$ and $h_{\Delta x}$ for $\Delta x = 1$.

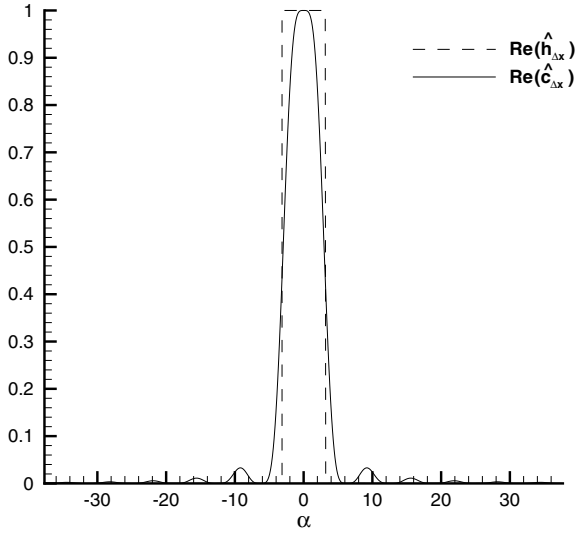

Fig. 4. $\hat{c}_{\Delta x}$ and $\hat{h}_{\Delta x}$ for $\Delta x = 1$.

That means interpolation creates very high wavenumbers which do not exist in f. However, we can note that the zeros of $\hat{c}_{\Delta x}$ are of the form $\alpha = 2\pi n/\Delta x$ with $n \neq 0$. As a consequence, the low wavenumbers of f create some disturbances of very small magnitudes in opposition to its high wavenumbers. The Section 3.3 explains how these very high wavenumber disturbances appear in the band-width of the second mesh.

3.3. Interpolation on a second mesh

Interpolation is used to initialize a second mesh, leading to the need to discretize $\mathscr{I}(f)(x)$. Eq. (27) showed us that a discretization "periodizes" the Fourier transform of a function, so we must go on the analysis to understand the link between the Fourier transform of a function on the first and the second mesh. To stay in the framework of the signal theory, we assume that the second mesh is of the form $x'_n = n\Delta x' + d$ where $-\Delta x/2 \leqslant d < \Delta x/2$. We note g_d the discretization of $\mathscr{I}(f)$ on this second mesh.

$$g_d(x) = \sum_{n=-\infty}^{\infty} \mathscr{I}(f)(n\Delta x' + d)\delta(x - n\Delta x' - d) \tag{28}$$

To be consistent, we assume that the support of $\hat{f}$ is included in $]-\pi/\Delta x', \pi/\Delta x'[$. The Fourier transform of g_d has the following analytical expression:

$$\begin{aligned} &\hat{g}_d(\alpha) = \frac{1}{\Delta x'} \sum_{m=-\infty}^{\infty} \mathrm{e}^{-\mathrm{i}\frac{2\pi m}{\Delta x'}d} \widehat{\mathscr{I}(f)}\left(\alpha - \frac{2\pi m}{\Delta x'}\right) \\ &\quad\Longleftrightarrow \\ &\hat{g}_d(\alpha) = \frac{1}{\Delta x'} \sum_{m=-\infty}^{\infty} \mathrm{e}^{-\mathrm{i}\frac{2\pi m}{\Delta x'}d} \hat{c}_{\Delta x}\left(\alpha - \frac{2\pi m}{\Delta x'}\right) \hat{f}_d\left(\alpha - \frac{2\pi m}{\Delta x'}\right) \end{aligned} \tag{29}$$

Ideally, we would have $\hat{g}_d = 1/\Delta x' \hat{f}$ on $]-\pi/\Delta x', \pi/\Delta x'[$. One can prove that the sole case in which it happens is $\Delta x' = \Delta x$ and $d = 0$, *i.e.* without interpolation. The fact that $\widehat{\mathscr{I}(f)}$ does not have its support included in $]-\pi/\Delta x,\ \pi/\Delta x[$ involves a phenomenon named aliasing or spectrum overlap in $\hat{g}_d$. The spurious modes created by interpolation appear now with wavenumbers belonging to $]-\pi/\Delta x', -\pi/\Delta x'[$, that means they cannot be all filtered. Besides, we can remark that in opposite to $\widehat{\mathscr{I}(f)}$, dephasing appears if $d \neq 0$, but it is important to notice that the interpolation itself does not create dephasing while the discretization of the interpolated function does. In the general case, since $\hat{g}_d$ is a periodization of $\widehat{\mathscr{I}(f)}$, interpolation error is minimized for low wavenumber functions.

However, there are interesting particular cases: $\Delta x = k\Delta x'$ and $\Delta x' = k\Delta x$ where k is an integer. If $\Delta x = k\Delta x'$, Eq. (29) is equivalent to:

$$\hat{g}_d(\alpha) = \frac{1}{\Delta x'}\left(\sum_{m=-\infty}^{\infty} \mathrm{e}^{-\mathrm{i}\frac{2\pi m}{\Delta x'}d}\hat{c}_{\Delta x}\left(\alpha - \frac{2\pi m}{\Delta x'}\right)\right)\hat{f}_d(\alpha) \tag{30}$$

Indeed, $\hat{f}_d$ is a $2\pi/\Delta x$ periodic function, since $\Delta x = k\Delta x'$, $\hat{f}_d$ is also a $2\pi/\Delta x'$ periodic function, yielding:

$$\hat{f}_d\left(\alpha - \frac{2\pi m}{\Delta x'}\right) = \hat{f}_d(\alpha) \quad \forall m \ \in]-\infty, \infty[$$

Thus, Eq. (30) can be deduced. One can notice that it is of the same form as Eq. (26). In this particular case, the wavenumbers of the spurious modes created by interpolation do not belong to $]-\pi/\Delta x, -\pi/\Delta x[$, that means they can all be filtered. Besides if $d = 0$, there is no dephasing on the wavenumbers of f. So, if $\Delta x > \Delta x'$, $\Delta x = k\Delta x'$ and $d = 0$ is the best configuration to use interpolation based on Lagrange polynomials. If $\Delta x' = k\Delta x$, Eq. (29) is equivalent to:

$$\hat{g}_d(\alpha) = \frac{1}{\Delta x}\left(\sum_{m=-\infty}^{\infty} \mathrm{e}^{-\mathrm{i}\frac{2\pi m}{\Delta x}d}\hat{c}_{\Delta x}\left(\alpha - \frac{2\pi m}{\Delta x}\right)\right)\frac{1}{\Delta x'}\hat{f}(\alpha) \quad \text{for } \alpha \in \left]-\frac{\pi}{\Delta x'}, \frac{\pi}{\Delta x'}\right[\tag{31}$$

In Eq. (29), each m can be rewritten in the form:

$$m = pk + q$$

with

$$0 \leqslant q < k$$

Since $\hat{f}_d$ is a $2\pi/\Delta x$ periodic function and $\Delta x' = k\Delta x$:

$$\hat{f}_d\left(\alpha - \frac{2\pi m}{\Delta x'}\right) = \hat{f}_d\left(\alpha - \frac{2\pi(pk+q)}{\Delta x'}\right) = \hat{f}_d\left(\alpha - \frac{2\pi q}{\Delta x'}\right)$$

Thus, Eq. (29) is equivalent to:

$$\hat{g}_d(\alpha) = \frac{1}{\Delta x'}\sum_{q=0}^{k-1}\left(\sum_{p=-\infty}^{\infty} \mathrm{e}^{-\mathrm{i}\frac{2\pi(pk+q)}{\Delta x'}d}\hat{c}_{\Delta x}\left(\alpha - \frac{2\pi(pk+q)}{\Delta x'}\right)\right)\hat{f}_d\left(\alpha - \frac{2\pi q}{\Delta x'}\right)$$

The support of $\hat{f}$ is included in $]-\pi/\Delta x', \pi/\Delta x'[$, so:

$$\hat{f}_d\left(\alpha - \frac{2\pi q}{\Delta x'}\right) = 0 \quad \text{for } q \neq 0 \text{ and } \quad \alpha \in \left]-\frac{\pi}{\Delta x'}, \frac{\pi}{\Delta x'}\right[$$

Thus, Eq. (31) can be deduced. In that configuration, no spurious mode appears, there is only dephasing if $d \neq 0$. Remark: for the previous result, the hypothesis $\hat{f} \in]-\pi/\Delta x', -\pi/\Delta x'[$ is fundamental otherwise there are aliasing troubles.

3.4. Numerical examples

The purpose of this section is to illustrate results presented above. We consider a family of functions of the form (see Fig. 5):

$$f_k(x) = \cos\left(\frac{k\pi}{16}x\right)\exp\left(-\left(\frac{x}{16}\right)^2\right) \quad k \in [0, 14] \tag{32}$$

The Fourier transform of f_k is:

$$\hat{f}_k(\alpha) = \frac{1}{2}\left(\hat{f}\left(\alpha - \frac{k\pi}{16}\right) + \hat{f}\left(\alpha + \frac{k\pi}{16}\right)\right) \tag{33}$$

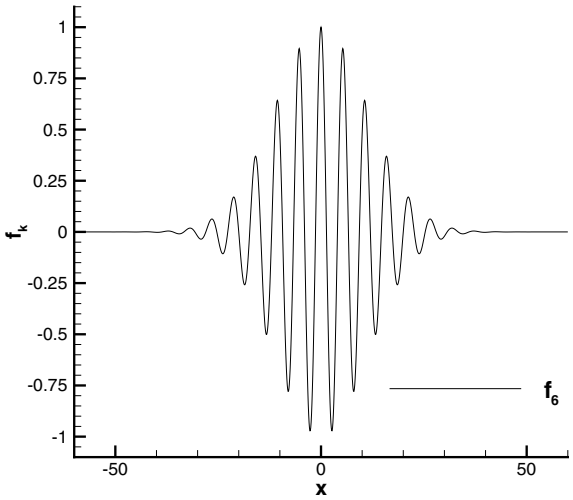

Fig. 5. f_6 typical function used for numerical tests.

where

$$\hat{f}(\alpha) = 16\sqrt{\pi}\exp\left(-\frac{(16\alpha)^2}{4}\right) \tag{34}$$

$\hat{f}_k$ is a real function with support included in $]-\pi,\pi[$. In Fig. 6, $\hat{f}_k$ is displayed for all k. The functions f_k are discretized with a step of 1, then they are interpolated with Lagrange polynomials. The Fourier transform of the interpolated function $\mathscr{I}(f_k)$ is displayed in Fig. 7 for $k = 4$ and 14 in log scale. Plots with a log scale show that interpolation creates some high wavenumber modes whatever the initial function is. If the wavenumbers of the initial function are low (functions f_k with $k = 0,1,2,3$ and 4), spurious modes are not significant: the relative error between the magnitude of the greatest spurious mode and the maximum magnitude of $\widehat{\mathscr{I}(f_k)}$ is lower than 0.1%. Whereas for high wavenumber functions, those modes may be very important: the relative error is greater than 50% for $k = 14$. However, we can note that the ratio between static and acoustic pressure

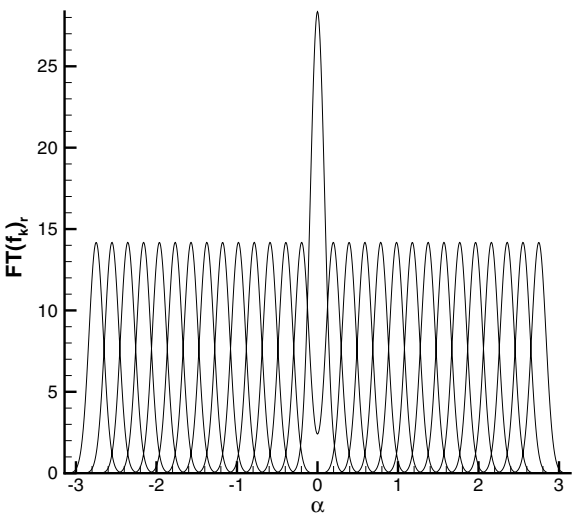

Fig. 6. Real part of $\hat{f}_k$ for $k \in [0,14]$.

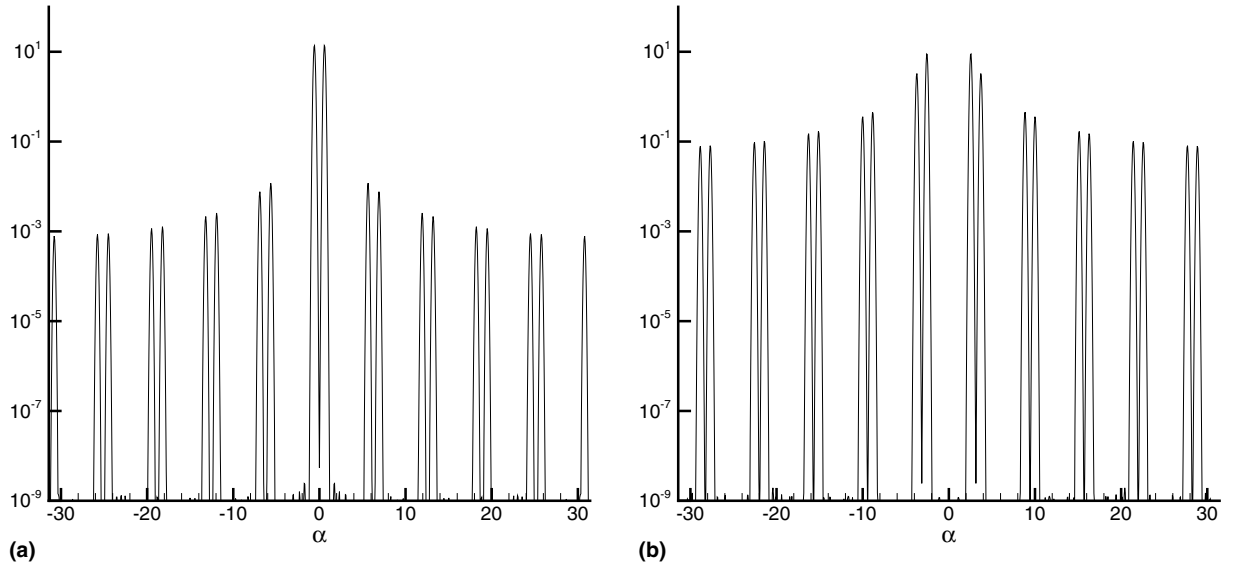

Fig. 7. Real part of $\widehat{\mathscr{I}(f_k)}$ in log scale for $k = 4$ (a), $k = 14$ (b); imaginary part of $\widehat{\mathscr{I}(f_k)}$ is zero.

is of the same order as the relative interpolation error of a low wavenumber signal, that explains why interpolation must be applied to perturbated variables.

Now, $\mathscr{I}(f_k)$ is used to initialize a second mesh of step $\Delta x'$, we note $g_{k,d}$ the discretized function. We have chosen two values for $\Delta x'$, one for a general case $\Delta x' = 2/3$, another one for a particular case $\Delta x' = 2$. For both the two cases $d = 0$ ($d \neq 0$ just creates dephasing). The Fourier transform of $g_{k,d}$ is then a real function as $\widehat{\mathscr{I}(f_k)}$ is.

In Fig. 8 for $\Delta x' = 2/3$, the real part of $\hat{g}_{k,d}$ is displayed for several k. We can observe the phenomenon predicted by theory, in particular some spurious modes can appear in $]-\pi, \pi[$.

The real part of $\hat{g}_{k,d}$ for $\Delta x' = 1/2$ is displayed in Fig. 9. In this particular case, we observe that none of the spurious modes belongs to $]-\pi, \pi[$. As a consequence, they can be filtered.

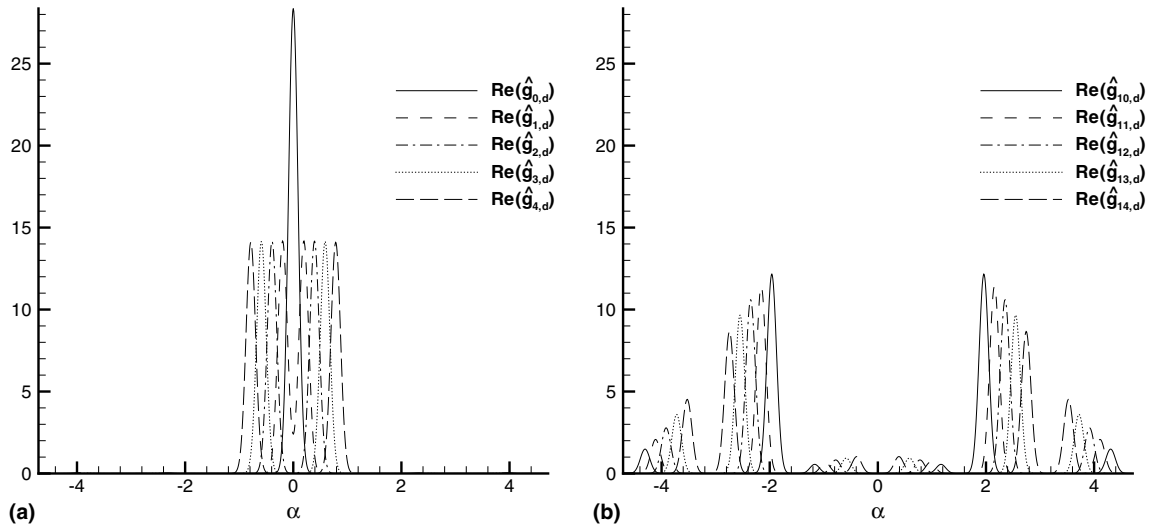

Fig. 8. Fourier transform of $g_{k,d}$ for $\Delta x' = 2/3$.

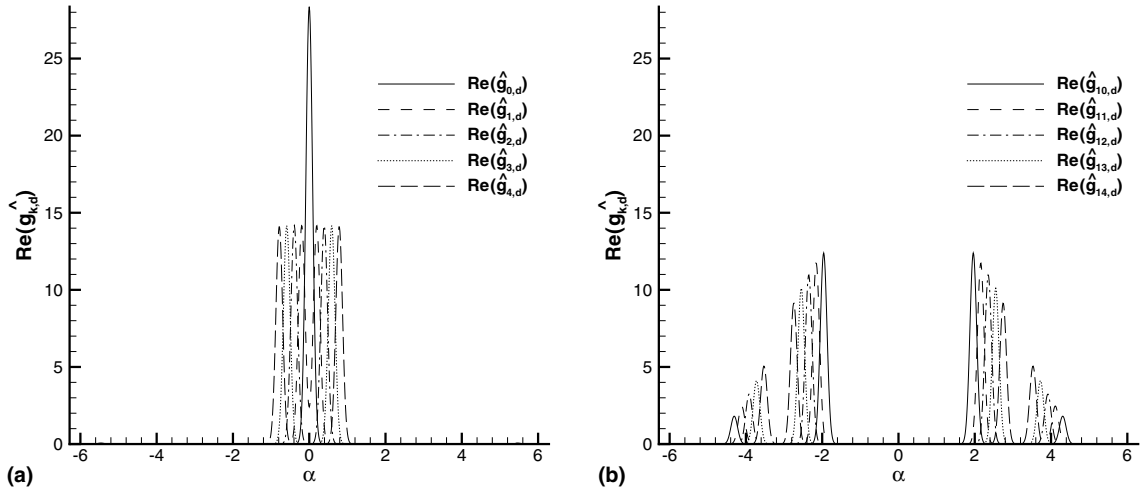

Fig. 9. Fourier transform of $g_{k,d}$ for $\Delta x' = 1/2$.

3.5. Conclusion

The theoretical analysis has shown that the interpolation creates some spurious modes for each wavenumber of the signal, but the lower the wavenumber is, the lower the magnitude of spurious mode is. In the general case, the spurious modes created cannot be all filtered because their wavenumbers belong to the whole band width of the mesh. This analysis has shown us what are the optimal conditions to apply this interpolation. The next two sections will now present some practical applications of the method to CFD/CAA coupling (Section 4) and CAA/CAA coupling (Section 5) in a complex geometry.

4. Application: cylinder noise

In a first step, the method has been carefully assessed on reference simple cases such as harmonic pulses (not shown here). The test case considered here consists in simulating the vortex shedding behind a cylinder and capturing the generated acoustic wave in farfield. This application illustrates the direct simulation approach for the prediction of the radiation of the aeroacoustic sources of the flow.

4.1. Configuration

The main parameters of the configuration are: $Re_D = 100$, $Ma = 0.15$ where D is the diameter of the cylinder centered at $x_0 = y_0 = 0$. Sherer and Scott [6] have tested the coupling method they proposed in a close configuration. However, their purpose was different, it was to properly capture the vortex shedding on the Cartesian grid, while our purpose here is to predict the farfield noise generated by the flow around the cylinder. Experience has shown that the sources of the generated acoustic waves are located just above and below the cylinder, and act as a dipole. In this configuration, the Strouhal number of the acoustic wave computed from numerical simulations [27–29] is 0.166. It corresponds to a wavelength varying from $34D$ to $46D$ between upstream and downstream parts of the domain. For this test, the characteristic scale difference between the hydrodynamic flow and the acoustic waves is very high. This disparity appears in the computational grids, indeed the height of the smallest cell of the body-fitted grid is $5 \times 10^{-3} D$ while a spatial increment of $3D$ would be sufficient to propagate the acoustic waves on the Cartesian mesh. Four simulations are performed with two different Cartesian grids. The curvilinear grid is defined such that the acoustic wave is well propagated up to $16D$ away from the cylinder. For these simulations, the Navier–Stokes equations (Eq. (1)) are used to simulate the unsteady flow on the body fitted grid and to propagate the acoustic wave on the Cartesian mesh. The numerical schemes defined in Section 2 are used to discretise them. Some classical boundary conditions based on the characteristic theory [30] have been used to minimize numerical reflections.

4.2. Cartesian grid description

The mesh size of the first uniform Cartesian grid is $0.75D$ in each direction. With such a mesh size, the number of points per wavelength is larger than 50. It is much more what is necessary knowing that eight points per wavelength are sufficient for a good numerical accuracy with the schemes used. But a much larger spatial increment cannot be taken because the Cartesian grid must be refined enough to handle the hydrodynamic fluctuations in the wake. With such a spatial increment, a spatial period of the vortex shedding represents about four points per wavelength. It can be noticed that it is not sufficient to ensure a good approximation of the different operators by the numerical scheme. In this condition, the hydrodynamic fluctuations will be damped on the Cartesian grid. However, the aim is here to propagate the acoustic waves on this grid, and we assume that these fluctuations have no major influence on the directivity of the aeroacoustic sources. The dimensions of the Cartesian grid are $279D \times 279D$. With this grid, three different coupling areas have been considered. The first one has a closed shape (simulation 1) and it intercepts the wake of the cylinder as shown in Fig. 10. This coupling area has been defined such that its outside boundary is located near the limit of the validity domain of the curvilinear mesh – acoustic waves are well propagated on the curvilinear grid up to 16 diameter – and it contains enough Cartesian points in each direction for the coupling procedure. The two other areas have an open shape and do not cross the wake of the cylinder. They are characterized by a different half opening angle, for one it is 50° (simulation 2) for the other 70° (simulation 3) (see Fig. 10). With open coupling areas, the physical flow cannot be computed for all Cartesian points. According to the location of the aeroacoustic source that is known in this configuration, the flow computed on the Cartesian points in the area corresponding to the opening angle of the coupling zones is supposed not to be valid (see Fig. 11).

The spatial increment of the second Cartesian grid, used in simulation 4, is $0.1D$. It is about eight times smaller than the one of the first Cartesian mesh. Its dimensions are $60D \times 60D$. The coupling area used in the simulation 4 is displayed in Fig. 12. It has been chosen such that in this area, the size of the Cartesian cells is the same order as the curvilinear ones. Since the Cartesian grid is very fine with respect to the hydrodynamic fluctuations in the wake (about 26 points per spatial period of the vortex shedding), sponge areas that consist in Cartesian grids progressively stretched in one direction have been used to damp the pressure fluctuations before they reach the boundaries of the computational domain. The features of the different simulations are summarized in Table 1.

4.3. Results

Simulation 1 failed to capture the physics of the flow as shown in Fig. 13. Even though the vortex shedding is well captured on the Cartesian mesh as in Sherer and Scott's configuration [6] and even if the cylinder dipolar source seems to have been captured on the Cartesian grid, there is a spurious source that appears in the coupling area around the wake, whose magnitude is the same order as the physical source on the cylinder. In the coupling area, the number of points for a spatial period of the vortex shedding is about 4 on the

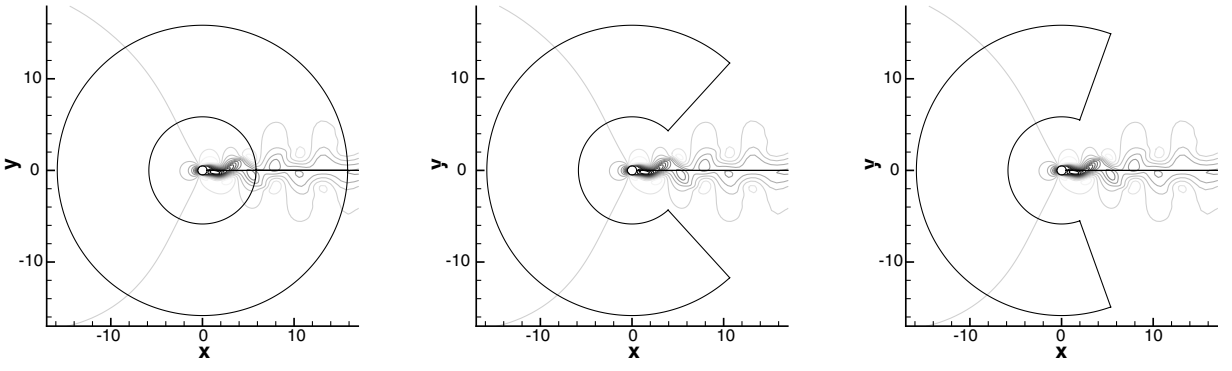

Fig. 10. Coupling region for the simulations 1, 2 and 3 from left to right, respectively.

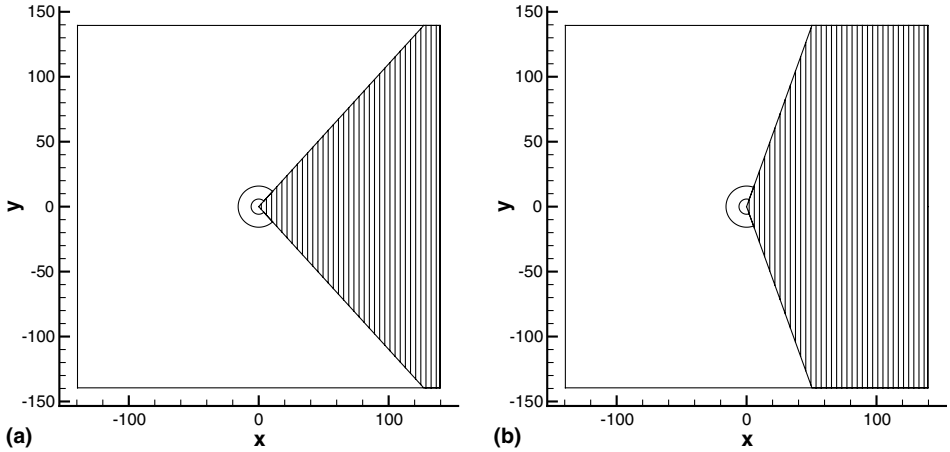

Fig. 11. Flow not valid on Cartesian points in gray area for simulations 2 and 3.

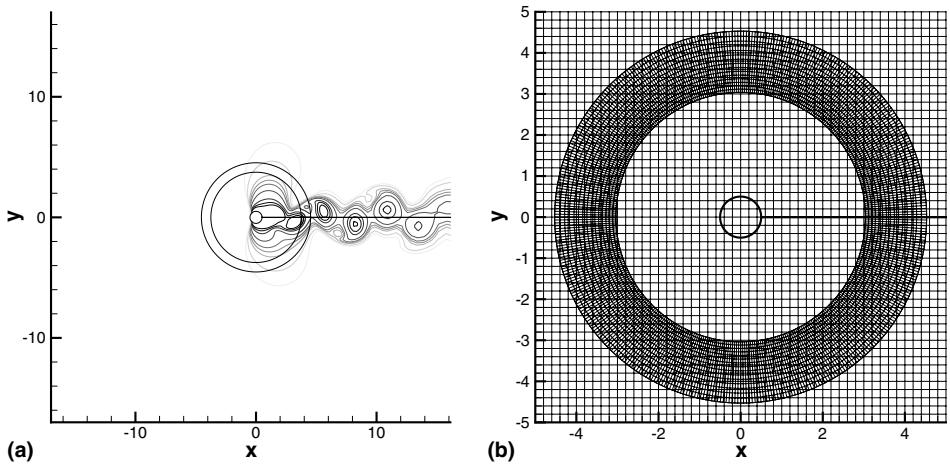

Fig. 12. Coupling zone defined on the curvilinear mesh for the simulation 4 using the second Cartesian grid (only every other grid point is shown on b).

Table 1
Main features of the four simulations

	Cartesian grid size	Cartesian grid dimensions	Coupling area	Sponge areas
Simulation 1	$0.75D$	$279D \times 279D$	Closed	No
Simulation 2	$0.75D$	$279D \times 279D$	Open (50°)	No
Simulation 3	$0.75D$	$279D \times 279D$	Open (70°)	No
Simulation 4	$0.1D$	$60D \times 60D$	Closed	Yes

Cartesian mesh and about 8 for the curvilinear one. According to the theoretical analysis performed in the previous section, the interpolation of hydrodynamic fluctuations and an aliasing phenomenon have generated spurious modes whose magnitudes are of the same order as the acoustic fluctuations. So, the acoustic field is strongly affected resulting in the creation of the spurious dipole. The result of the simulations 2 and 3 will allow to assess this hypothesis since the coupling area does not cross the wake for the two other simulations. It can be noticed that there are troubles with the boundary condition on the symmetry plane of the configuration at the downstream boundary. As a matter of fact, a low pressure region (in black in Fig. 13) appears. For the simulations 2 and 3, one observes a dipolar radiation on the Cartesian mesh with an apparent source

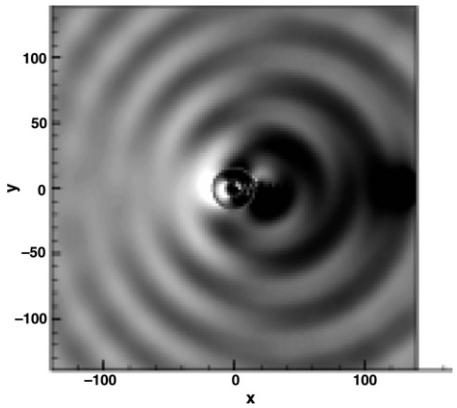

Fig. 13. Simulation 1: pressure fluctuations, range from −20 to 20 Pa around p_∞.

located around the cylinder (see Fig. 14). This confirms that the interpolation of the hydrodynamics fluctuations in the wake was responsible for the spurious acoustic dipole that has appeared in the first simulation. It can also be noticed that the boundary condition still induces some troubles. In Fig. 15, instantaneous pressure fluctuations around p_∞ of simulation 4 can be observed. The black circle is the interface between the curvilinear grid and the Cartesian one. A part of the fluctuations in the sponge areas is also displayed. The damping effect on the wake behind the cylinder is to be noticed. For this simulation, the spurious dipole is no longer observed.

In Fig. 16, the temporal pressure signal at the point $(-25;-25)$ is displayed for simulations 2, 3 and 4. Five periods can be observed, from which the Strouhal number of the acoustic source can be computed. Its value is 0.164 for each simulation. It is a little smaller than the reference one previously quoted. However, the same Strouhal number is obtained on the curvilinear grid, so the coupling method is not responsible for this small difference.

A reference simulation of the cylinder noise in the configuration described above has been computed on a curvilinear mesh refined such that the acoustic is well propagated up to $R = 30D$. The computation of the statistical variables has been done over six periods of the vortex shedding. In Fig. 17, the directivity diagrams of simulations 2, 3 and 4 are compared with the reference solution. It is seen that the rms pressure profiles of simulations 2 and 3 match the reference for the assumed valid angles (between the vertical lines) with a difference lower than 2 dB except for angles around 180° where the difference is about 7 dB. It corresponds to the symmetry plane of the configuration upstream the cylinder. It can also be observed that, except for the ends of the angle interval, the difference of the rms pressure of the simulation 4 to the reference remains lower

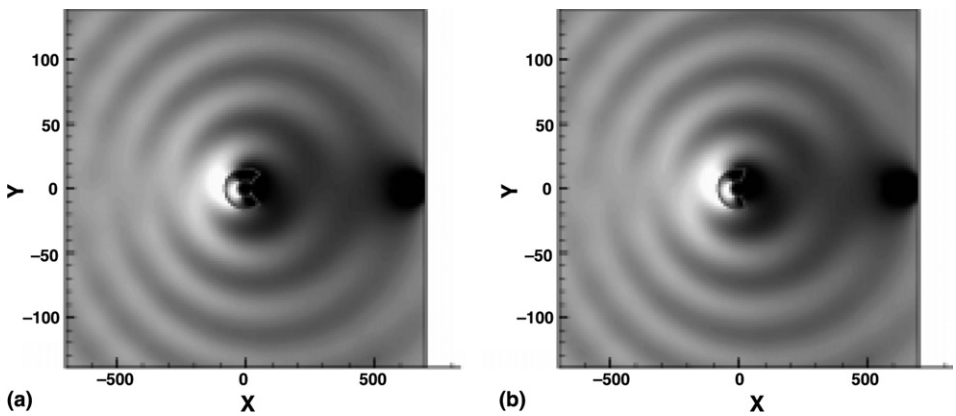

Fig. 14. Pressure fluctuations, range from −20 to 20 Pa around p_∞: (a) simulation 2; (b) simulation 3.

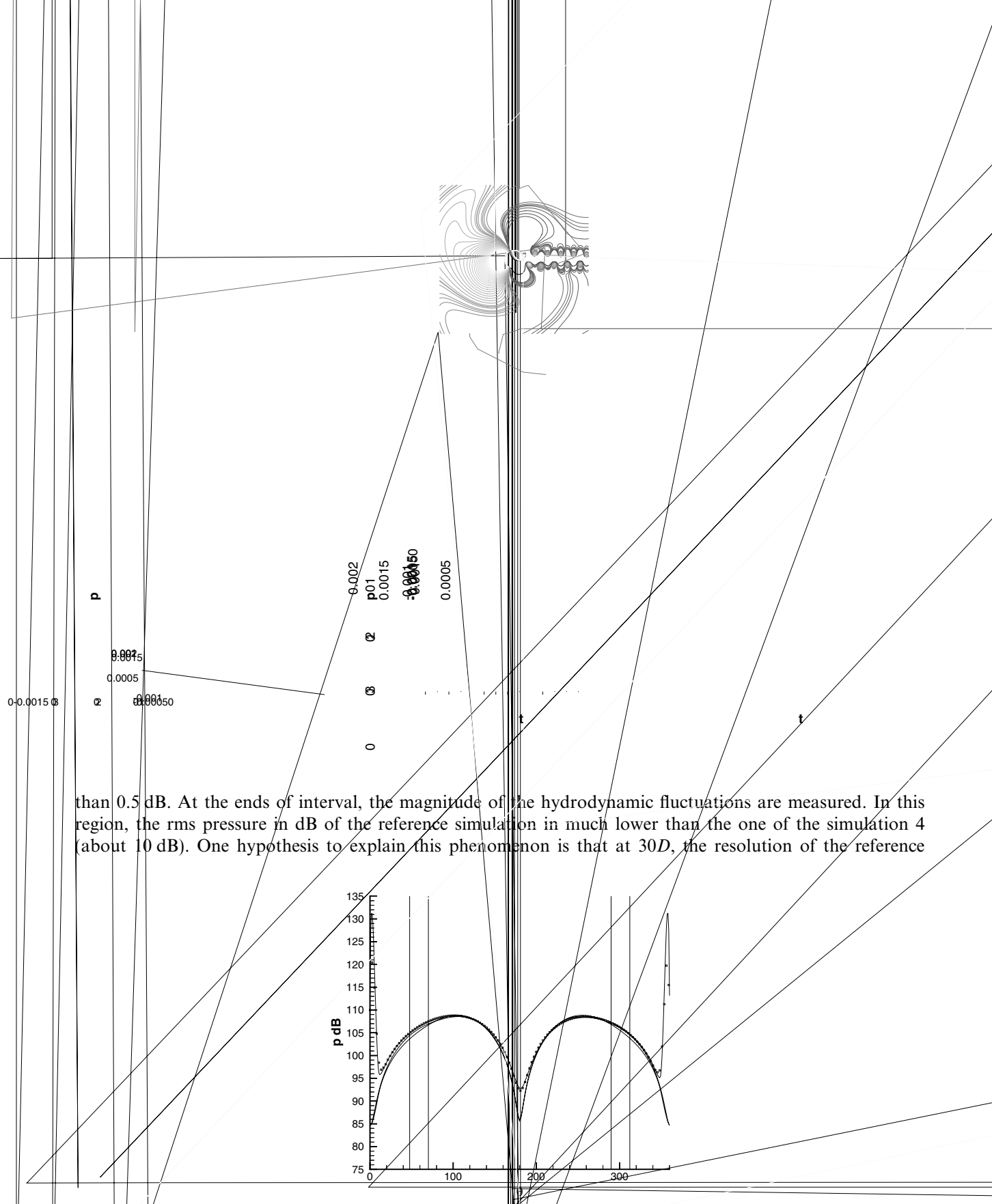

than 0.5 dB. At the ends of interval, the magnitude of the hydrodynamic fluctuations are measured. In this region, the rms pressure in dB of the reference simulation in much lower than the one of the simulation 4 (about 10 dB). One hypothesis to explain this phenomenon is that at $30D$, the resolution of the reference

Fig. 17. Rms pressure in dB function of θ at $R = 30D$ reference, circle symbol; simulation 2, dash-dotted line; simulation 3, long-dashed line; simulation 4, solid line.

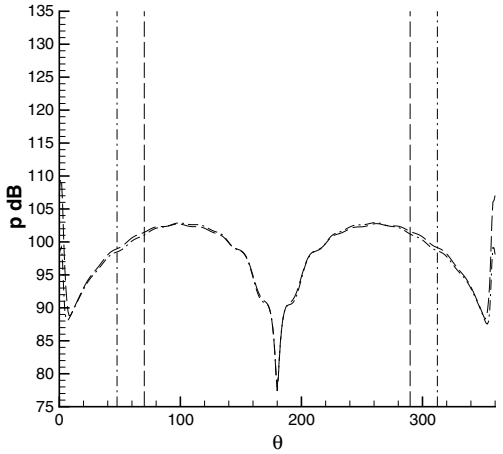

Fig. 18. Rms pressure in dB function of θ at $R = 110$D, - · - simulation 2, – – simulation 3.

curvilinear mesh in the streamwise direction is low with about 4 points per wavelength of hydrodynamic fluctuations. This means that these fluctuations are damped in the reference simulation. On the contrary, the Cartesian grid has a higher resolution, and so the numerical dissipation is lower. Once again, excepted in the wake region, it can be noticed that it is for the angles around 180° the rms pressure error is the greater. At $R = 110D$, a directivity diagram can be computed only for simulations 2 and 3. Indeed for computational cost reasons, the Cartesian grid of the simulation 4 is not as large as the one of the two other simulations. At this distance (Fig. 18), the rms pressure predicted by both simulations are almost identical. So, it can be observed that the differences between the coupling areas of the simulation 2 and 3 do not have major influence on the farfield noise radiated. However, it can be noticed that small rms pressure fluctuations appear on the diagrams. It seems that the boundary conditions used could not prevent all acoustic reflections. It may be thought that these reflections can be responsible for the difference of the rms pressure in dB between simulations 2 and 3 and the reference one that have been observed in Fig. 17.

4.4. Conclusion

It was observed in simulation 1 that the interpolation of hydrodynamic fluctuations can generate spurious acoustic waves. Guénanff [2] has encountered the same phenomenon with the mesh refinement method he has developed. Providing that areas with significant hydrodynamic fluctuations have been avoided, a part of the farfield acoustic radiation could have been computed with the simulations 2 and 3. However, the quality of the computed acoustic radiation is not very satisfactory. Besides, the knowledge we had of the solution was necessary to define a "good" coupling area. This might be seen as a limitation in the use of the grid coupling method. Simulation 4 with a much more refined Cartesian grid did not make a spurious dipole appear in the wake. This result is coherent with the theoretical study that has shown that the interpolation error is proportional to the wavenumber of the signal. By refining the Cartesian grid and the curvilinear cells in the coupling area (by getting it closer to the cylinder), the interpolation errors have been reduced. The directivity computed at $30D$ is more accurate than for the simulations 2 and 3. So, the one-way coupling method has allowed to predict the noise radiated by the flow around the cylinder. But it is to be noticed that a high resolution for the hydrodynamic scales on the Cartesian grid must be used (about 26 points per wavelength of the vortex shedding) in order to prevent the generation of spurious acoustic modes by the interpolation in this area.

5. High lift wing profile application

The purpose of this section is to assess the applicability of the proposed coupling method for industrial configurations. We consider here a high-lift wing profile. This configuration was the object of various

experimental [31] and numerical [32–35,2] studies. This study is based on the one proposed by Guénanff [2] to evaluate his mesh refinement method. The main source of the aeroacoustic noise is represented thanks to an analytical model, then two simulations are carried out, one without mean flow and another one with the mean flow computed by Ben Khelil [35] using RANS.

5.1. Configuration description

The profile corresponds to a 1/11th scale three element wing, of chord 6.5 m, with deployed slat and flap. The slat and flap deflection angles are, respectively, 32° and 17°. The mean flow is the one computed by Ben Khelil [35] using RANS, corresponding to a freestream velocity of 65.51 m/s, or equivalently to a Mach number of 0.2. The Reynolds number based on the wing chord in cruise configuration is $Re = 2.55 \times 10^6$. The angle of attack of the main wing body is equal to 4° (see Fig. 19).

The mesh around the profile is composed of 14 domains. The set of curvilinear domains contains about 165,000 cells (see Fig. 20).

The simulations of Choudhary et al. [32], Labourasse [34] and Ben Khelil [35] showed that the main source of the aeroacoustic noise around the slat has a frequency of 30 kHz and is located just behind the upper trailing edge. We model it using a harmonic monopolar acoustic source of the form:

$$s(x,t) = \sin(2\pi f t)\mathrm{e}^{-\frac{|x-x_s|^2}{b^2}} \tag{35}$$

where f is the frequency of the source, x_s its coordinates ($x_s = (0.0083,\ 0.03)$) and b determinates its width ($b = 0.003$). This forcing is applied on the curvilinear grids only. The acoustic wave propagates on the uniform Cartesian grid beyond the coupling area defined near the profile (see Fig. 21). The mesh size of the Cartesian grid is 0.0014 in each direction corresponding to 8 points per wavelength. The dimensions of this grid have be chosen such that the acoustic wave can be propagated up to one chord in each direction (see Fig. 22). The Cartesian domain contains 1,680,000 cells.

Two simulations have been carried out. For the first one, the mean velocity flow is set to zero in order to compare the results to those obtained with the commercial software SYSNOISE based on Boundary Element Method. For the second simulation, the RANS mean flow computed by Ben Khelil is used. It is characterized by the presence of a separation bubble in the cavity behind the slat (see Fig. 23) as previously shown by Choudhari et al. [32].

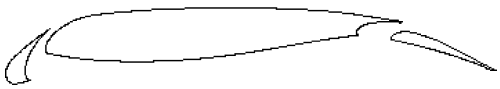

Fig. 19. High lift wing profile.

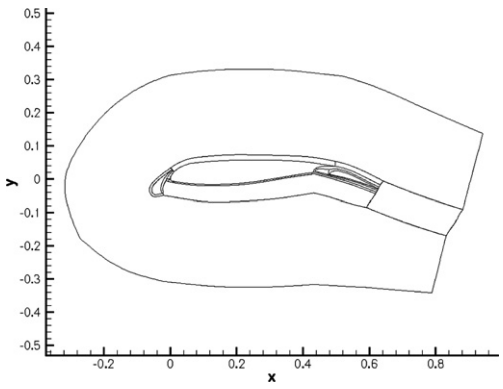

Fig. 20. Curvilinear mesh boundaries.

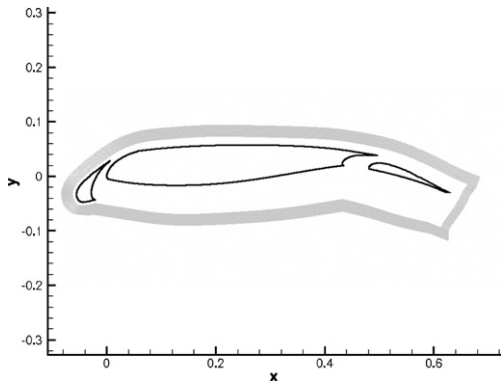

Fig. 21. Coupling area.

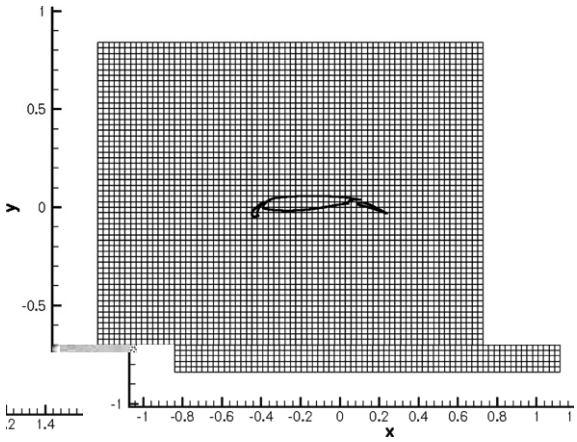

Fig. 22. Cartesian grid, one point on 20.

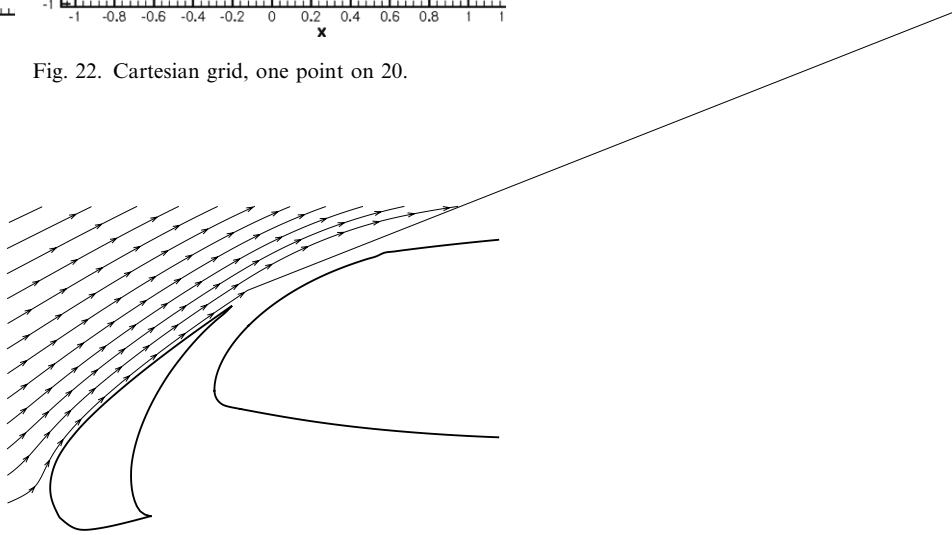

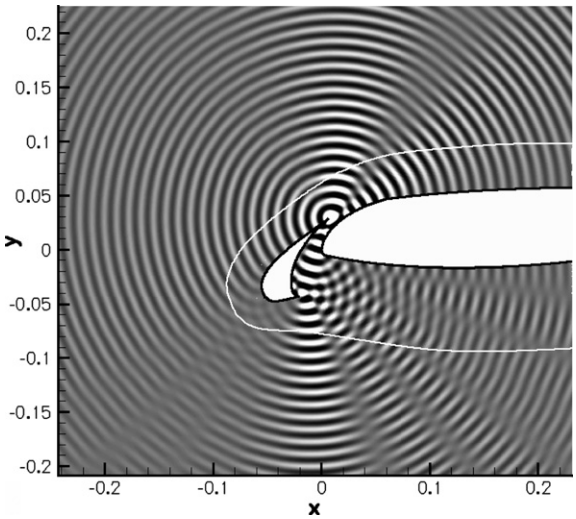

Fig. 24. Unsteady pressure fluctuations between −10 and 10 Pa. Outside the white line, values from Cartesian domain are plotted, inside values from curvilinear domains.

For these simulations, the Euler equations in a perturbation form are solved. The numerical schemes are the same as in the cylinder application. In addition to the non-reflective boundary conditions of Thompson [30], a buffer area (grid stretching) around the Cartesian grid has been used to damp acoustic waves reaching the boundaries.

5.2. Results

5.2.1. Simulation with a mean flow at rest

After 10,000 time steps, a statistically steady state is reached. Fig. 24 shows the instantaneous pressure fluctuations. Inside the region demarcated by the white line, fluctuations from the curvilinear domains are plotted, while those coming from the Cartesian domain are displayed outside. The rms pressure is computed over 45

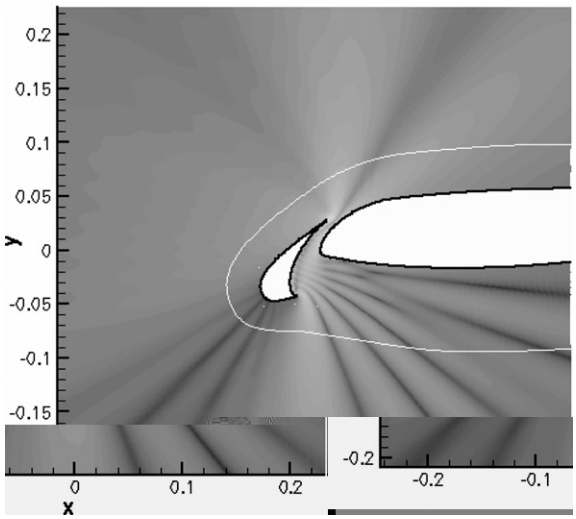

Fig. 25. Rms pressure around the slat, fluctuations between 60 and 140 dB. Outside the white line, values from Cartesian domain is plotted, inside values from curvilinear domains.

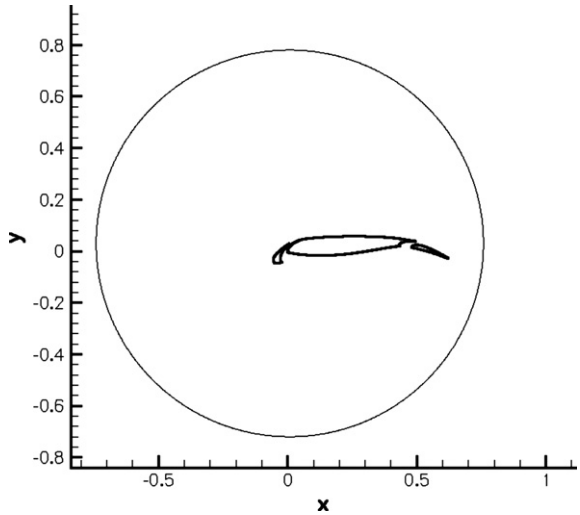

Fig. 26. Circle on which the directivity diagram is computed.

periods of the source. It is displayed in Fig. 25 around the slat. One can then observe the directivity of the source without mean flow. In both figures, a perfect continuity between the curvilinear and Cartesian meshes is observed, proving that the acoustic waves are accurately interpolated. The rms pressure allows us to compute the directivity of the source. It is computed on a circle centered on the source with a radius of 0.75 m (see Fig. 26). It has also been computed with the commercial software SYSNOISE based on Boundary Element Method. After a proper normalization (the radiated acoustic powers must be equal), results can be compared. The two computed directivities are plotted in Fig. 27, showing a very good agreement.

The maximum error is about 2 dB and we can suppose that this difference can be explained by different shapes of the acoustic source used for the two computations (pointwise source for BEM). In the area behind the flap, differences are about 15 dB. We found that the curvilinear mesh was responsible for this. In this region, the distance between two points is about 0.0023 m whereas the space step of the Cartesian grid (well

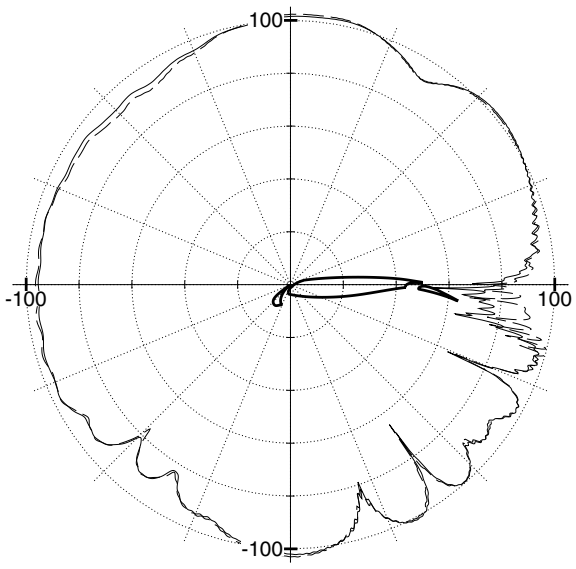

Fig. 27. Directivity diagram at 0.75 m from the source. In solid line, the rms pressure in dB our the simulation, in long dash line, the one from a simulation based on boundary element method.

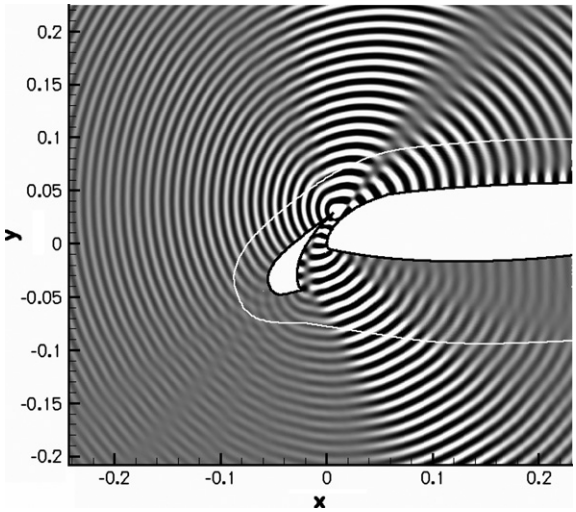

Fig. 28. Unsteady pressure, fluctuations between −5 and 5 Pa. Outside the white line, values from Cartesian domain are plotted, inside values from curvilinear domains.

suited to propagate the 30 kHz acoustic waves) is 0.0014 m. The curvilinear mesh is thus not fine enough in this region to properly propagate the acoustic wave before it is interpolated on the Cartesian grid.

5.2.2. Simulation with a steady RANS mean flow

After 15,000 time steps, a statistically steady state is reached. In Fig. 28, we can observe the pressure fluctuations around the slat and in Fig. 29, the rms pressure computed over 45 periods is plotted in dB scale.

As pointed out by Guénanff [2], one can see that the mean flow significantly modifies the radiation of the source below the wing. In Fig. 30, the directivities of the source at $0.75m$, with and without mean flow, are plotted. We can then see the influence of the mean flow. We can however observe some oscillations of the pressure contour for the simulation with RANS mean flow. It seems that the RANS mean flow is responsible for this. The near field mean pressure is correctly captured (see Fig. 31) while some wiggles are present in the far-field (see Fig. 32).

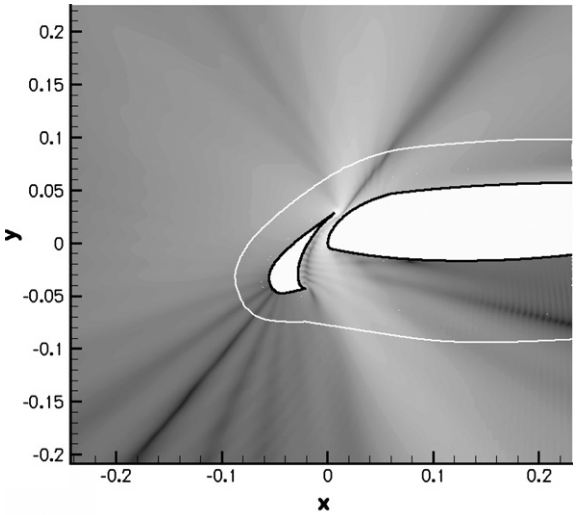

Fig. 29. Rms pressure around the slat, fluctuations between 60 and 140 dB. Outside the white line, values from Cartesian domain are plotted, inside values from curvilinear domains.

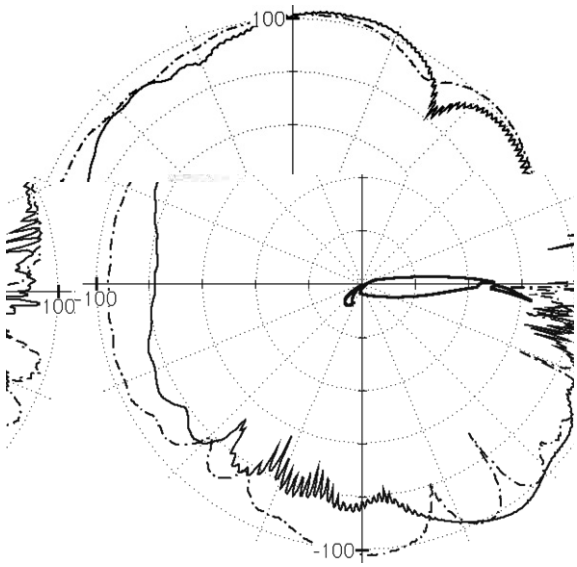

Fig. 30. Directivity diagram at 0.75 m away from the source. Solid line: rms pressure in dB from the simulation with RANS mean flow; dotted line: simulation without mean flow.

To check this hypothesis, a partial directivity diagram has been computed at 0.2 m from the source – at this distance, the circle goes through the profile. It is plotted on Fig. 33, together with the directivity computed at 0.75 m. We can observe that the oscillations do not appear at short distance from the profile, which comes to support our hypothesis.

5.3. Conclusion

The coupling method has been assessed on the simulation with a mean flow at rest by comparing the results to those of a reference simulation using a Boundary Element Method approach. Then, the simulation with a non-uniform RANS mean flow has allowed to observe the influence of the mean flow on the directivity of the source. The second simulation has also pointed out the fact that attention must be paid in the computation of

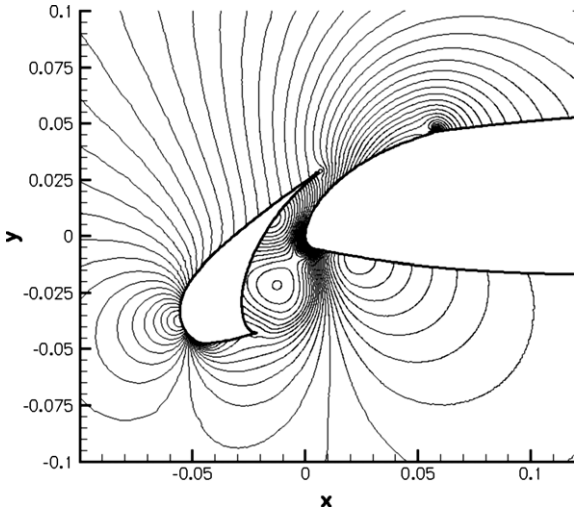

Fig. 31. Iso-pressure contours obtained in the RANS simulation, 80 isovalues between 89,000 and 101,000 Pa.

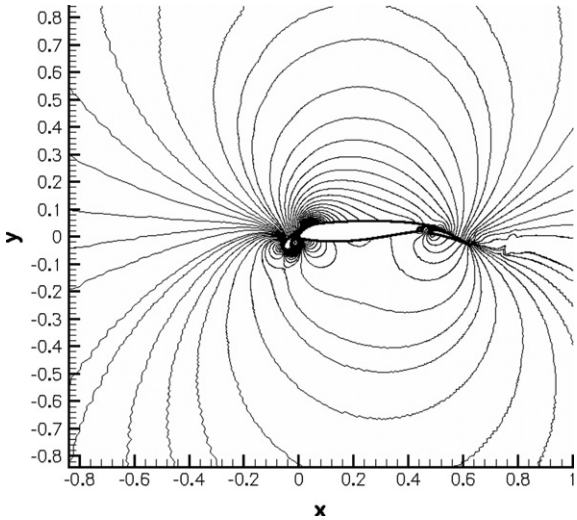

Fig. 32. Iso-pressure contours obtained in the RANS simulation, 80 isovalues between 89,000 and 101,000 Pa.

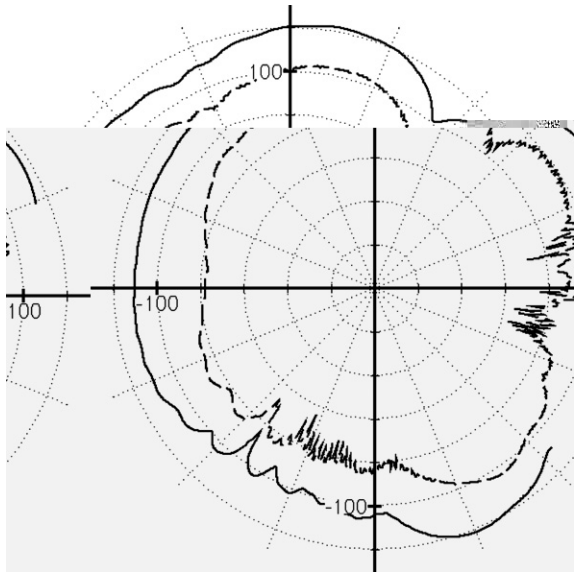

Fig. 33. Directivity diagram from the simulation with RANS mean flow. Solid line, the rms pressure in dB at 0.2 m away from the source; long dash line: the one at 0.75 m.

the mean flow for acoustic studies. It can be noticed here that the use of an analytical model to represent the source of the main aeroacoustic noise and the use of a RANS mean flow have allowed to get over the difficulties linked to the disparity of the hydrodynamic and acoustic scales.

6. Conclusion and future works

An overlapping grid method for one-way coupling has been presented here. It consists in a Chimera-like method which has been adapted to the numerical schemes required for CAA. At the interface between the Cartesian and curvilinear domains, an interpolation based on 4th order Lagrange polynomials is used to transfer information from the curvilinear grid to the Cartesian one.

Lagrange polynomials are used in most high-order overlapping grid methods already developed. Here, a theoretical analysis of this interpolator has been proposed in the framework on the signal theory. It has been shown that interpolation based on Lagrange polynomials can be seen as an approximation of the Shannon's interpolation function which is the ideal one in the framework of this theory. The theoretical analysis has shown that Lagrange interpolation is responsible for the creation of spurious modes, and that their magnitude depends on the wavenumbers of the signal: the higher the wavenumbers are, the greater the magnitude of the created spurious modes is. In the usual case, these spurious modes cannot be all filtered. However, some specific configurations have been exhibited for which they could be all suppressed.

The overlapping grid method has been used in two configurations which are more complex than those usually presented in the CAA literature. The first one is the simulation of the noise generated by the flow around a cylinder. The complexity comes here from the huge scale disparity between the hydrodynamic and acoustic fluctuations. It was then observed that interpolation in the wake could create a spurious acoustic source if the Cartesian mesh was not fine enough. More precisely, a very high resolution for the hydrodynamic scales has to be considered when defining the Cartesian grid even if the only purpose is the propagation of the acoustic waves.

For the second application, a high-lift wing profile in landing configuration has been considered. The complexity comes here from the geometry of the profile. The purpose of the application was the prediction of the farfield noise radiated by a model aeroacoustic source of the slat. Two simulations have been carried out: one with a mean flow at rest and a second one with a non-uniform turbulent mean flow. For the first one, results have been favorably compared to those obtained with a solver based on Boundary Element Method. For the second one, we could observe that the mean flow had a great influence on the directivity of the source below the wing as already pointed out by Guénanff [2]. This application shows that high-order overlapping grid methods are well adapted for configurations with a complex geometry as Chimera-like methods in CFD simulations.

The main conclusion of this work is twofold. First, it has been shown that the use of an overlapping grid method makes it possible to perform accurate aeroacoustic simulations around complex geometries thanks to the use of a background Cartesian grid for mid- and farfield acoustic wave propagation. This therefore allows us to investigate the effects of a non-uniform mean flow on acoustic propagation in some realistic cases (*i.e.* of engineering interest). The second point is that the use of interpolation techniques is responsible for the creation of spurious modes when a too important disparity is present between the characteristic scales represented by each of the two grids. It has been shown both by theoretical analysis and by performing coupled CFD/CAA simulations that the only efficient way to avoid such spurious modes to be generated is to refine both the two grids enough so that all the scales of interest are large when compared to the spatial increment. This becomes obviously a drastic constraint for CFD/CAA coupling where the scale disparity between the hydrodynamic and acoustic scales is huge. For this reason, it appears interesting for future studies to consider alternative approaches which introduce for CAA some equivalent source terms computed from the CFD results. By doing so, it will be ensured that the scale disparity problem will not be present anymore since all the hydrodynamic fluctuations in the CFD domain will simply be replaced by some source terms at the noise generation location. The characteristic scale associated to the interpolated information would then in this case be the wavelength of the acoustic phenomena, therefore making it possible to use much coarser grids to perform the propagation than if the hydrodynamic scales have to be accounted for. Such source terms may be directly derived from unsteady CFD calculations as proposed for instance by Billson et al. [36] or by Stochastic noise modeling as in the SNGR approach [37]. The possible coupling of such techniques with an overlapping grid method will be investigated in future studies.

References

[1] E. Manoha, C. Herrero, P. Sagaut, S. Redonnet, Numerical prediction of airfoil aerodynamic noise, AIAA Paper 2002-2573, 2002.

[2] R. Guénanff, Couplage instationnaire Navier–Stokes/Euler pour la génération et le rayonnement des sources de bruit aérodynamique, PhD thesis, Université de Rennes I, 2004.

[3] R. Guénanff, M. Terracol, E. Manoha, P. Sagaut, R. Lewandowski, Theoretical and numerical aspects of a multidomain high-order method for CAA, AIAA Paper 2003- 3117. Ninth AIAA/CEAS Aeroacoustics Conference, Hilton Head, May 2003.

[4] R. Guénanff, M. Terracol, Study of stabilization methods for computational aeroacoustic, Comptes Rendus Mécanique, 333(9), Académie des Sciences, Paris, September 2005.
[5] J.W. Delfs, CAA-simulation of aeroacoustic sources on overlapped grids, Second Aeroacoustic Workshop SWING, October 2000.
[6] S.E. Sherer, J.N. Scott, Development and validation of a high-order overset grid flow solver, AIAA Paper 2002-2733, 32nd AIAA Fluid Dynamics Conference and Exhibit, St Louis, June 2002.
[7] Y. Lee, J.D. Baeder, High-order overset method for blade vortex interaction, AIAA Paper 2002-0559, AIAA 40th Aerospace Sciences Meeting, Reno, January 2002.
[8] J.L. Steger, F.C. Dougherty, J.A. Benek, A Chimera grid scheme, ASME Mini-Symposium on Advances in Grid Generation, Houston, 1982.
[9] J.A. Benek, J.L. Steger, F.C. Dougherty, A flexible grid embedding technique with application to the Euler equations, AIAA Paper 1983–1944, 1983.
[10] G. Chesshire, W.D. Henshaw, Composite overlapping meshes for the solution of partial differential equations, J. Comput. Phys. 90 (1) (1990) 1–64.
[11] J.W. Delfs, An overlapped grid technique for high resolution CAA schemes for complex geometries, AIAA Paper 2001-2199, Seventh AIAA/CEAS Aeroacoustics Conference, Reno, May 2001.
[12] J. Yin, J. Delfs, Sound generation from gust–airfoil interaction using CAA-Chimera method, AIAA Paper 2001-2136, Seventh AIAA/CEAS Aeroacoustics Conference, Maastricht Netherlands, May 2001.
[13] C.K.W. Tam, K.A. Kurbatskii, An optimized extrapolation and interpolation method for computational aeroacoustics, AIAA Paper 2000-0218, January 2000.
[14] S.E. Sherer, J.N. Scott, Comparison of highly accurate interpolation methods, AIAA Paper 2001-0282, AIAA 39th Aerospace Sciences Meeting, Reno, January 2001.
[15] P.J. Morris, L.N. Long, A. Bangalore, Q. Wang, A parallel three-dimensional computational aeroacoustics method using nonlinear disturbance equations, J. Comput. Phys. 133 (1997) 56–74.
[16] E. Labourasse, P. Sagaut, Reconstruction of turbulent fluctuations using a hybrid RANS/LES approach, J. Comput. Phys. 182 (2002) 301–336.
[17] S.K. Lele, Computational aeroacoustics: a review, 35th Aerospace Sciences Meeting and Exhibit, Reno, 1997.
[18] C.K.W. Tam, Computational aeroacoustics: issues and methods, AIAA J. 33 (1995) 1788–1796.
[19] M.R. Visbal, D.V. Gaitonde, On use of higher-order finite-difference schemes on curvilinear and deforming meshes, J. Comput. Phys. 181 (2002) 155–185.
[20] C. Bogey, C. Bailly, A family of low dispersive and low dissipative explicit schemes for flow and noise computations, J. Comput. Phys. 194 (2004) 194–214.
[21] M. Terracol, E. Manoha, C. Herrero, E. Labourasse, S. Redonnet, P. Sagaut, Hybrid methods for airframe noise numerical prediction, Theor. Comput. Fluid Dyn. 19 (3) (2005) 197–227.
[22] S.E. Sherer, M.R. Visbal, Computational study of acoustic scattering form multiple bodies using a high-order overset grid approach, AIAA Paper 2003-3203, Ninth AIAA/CEAS Aeroacoustics Conference, Hilton Head, May 2003.
[23] J.A. Benek, J.L. Steger, F.C. Dougherty, P. Burning, Chimera: a grid embedding technique, Technical Report AEDC-TR-85-64, April 1986, Arnold Engineering Development Center.
[24] C.E. Shannon, Communications in the presence of noise, Proc. IRE 37 (January) (1949) 10–21.
[25] J. Whittaker, Interpolatory Function Theory, Cambridge Tracks in Math. and Math. Physics, 1935.
[26] S. Mallat, A Waveler Tour of Signal Processing, Academic Press, 1999 (Chapter 2).
[27] A. Burbeau, P. Sagaut, Simulation of a viscous compressible flow past a circular cylinder with high-order discontinous Galerkin methods, Comput. Fluids 31 (2002) 867.
[28] R. Franke, W. Rodi, B. Schonung, Numerical calculation of laminar vortex-shedding flow past cylinders, J. Wing Eng. Ind. Aerodyn. 35 (1990) 236–257.
[29] I. Lomtev, C.B. Quillen, G. Karniadakis, Spectral/hp methods for viscous for viscous compressible flows on unstructured 2D meshes, J. Comput. Phys. 144 (1998) 325.
[30] K.W. Thompson, Time dependant boundary conditions for hyperbolic systems, J. Comput. Phys. 68 (1987) 1–24.
[31] R. Davy, F. Moens, H. Remy, Aeroacoutic behavior of a 1/11 scale Airbus model in the open anechoic wind tunnel CEPRA 19, AIAA Paper 2002-2412, 2002.
[32] M. Choudhary, M.R. Khorrami, D.P. Lockard, H.L. Atkins, Slat cove noise modelling: a posteriori analysis of unsteady RANS simulations, AIAA Paper 2002-2468, 2002.
[33] M. Terracol, E. Labourasse, E. Manoha, P. Sagaut, Simulation of the 3d unsteady flow in a slat cove for noise prediction, AIAA Paper 2003-31110, Ninth AIAA/CEAS Aeroacoustics Conference, Hilton Head, May 2003.
[34] E. Labourasse, Reconstruction des fluctuations turbulentes par une approche hybride RANS/SGE. PhD thesis, ONERA, 32nd AIAA Fluid Dynamics Conference and Exhibit, St Louis, June 2002.
[35] S. Ben Khelil, Large eddy simulation of the flow around a slat with a blunt trailing edge, ICCFD3-2004, 2004.
[36] M. Billson, L.E. Erikson, L. Davidson, Acoustic source terms for linearized Euler equations in conservative form, AIAA J. 43 (4) (2005) 752–759, CPL 11492.
[37] C. Bailly, P. Lafon, S. Candel, Subsonic and supersonic jet noise predictions from statistical source models, AIAA J. 35 (11) (1997) 1688–1696.